

MAIN-BELT ASTEROIDS WITH WISE/NEOWISE: NEAR-INFRARED ALBEDOS

JOSEPH R. MASIERO¹, T. GRAV², A. K. MAINZER¹, C. R. NUGENT¹, J. M. BAUER^{1,3}, R. STEVENSON¹, AND S. SONNETT¹

¹ Jet Propulsion Laboratory/Caltech, 4800 Oak Grove Drive, MS 183-601, Pasadena, CA 91109, USA; Joseph.Masiero@jpl.nasa.gov, amainzer@jpl.nasa.gov, cnugent@jpl.nasa.gov, James.Bauer@jpl.nasa.gov, Rachel.A.Stevenson@jpl.nasa.gov, sarah.sonnett@jpl.nasa.gov

² Planetary Science Institute, Tucson, AZ, USA; tgrav@psi.edu

³ Infrared Processing and Analysis Center, Caltech, Pasadena, CA, USA

Received 2014 May 14; accepted 2014 June 25; published 2014 August 6

ABSTRACT

We present revised near-infrared albedo fits of 2835 main-belt asteroids observed by *WISE*/*NEOWISE* over the course of its fully cryogenic survey in 2010. These fits are derived from reflected-light near-infrared images taken simultaneously with thermal emission measurements, allowing for more accurate measurements of the near-infrared albedos than is possible for visible albedo measurements. Because our sample requires reflected light measurements, it undersamples small, low-albedo asteroids, as well as those with blue spectral slopes across the wavelengths investigated. We find that the main belt separates into three distinct groups of 6%, 16%, and 40% reflectance at 3.4 μm . Conversely, the 4.6 μm albedo distribution spans the full range of possible values with no clear grouping. Asteroid families show a narrow distribution of 3.4 μm albedos within each family that map to one of the three observed groupings, with the (221) Eos family being the sole family associated with the 16% reflectance 3.4 μm albedo group. We show that near-infrared albedos derived from simultaneous thermal emission and reflected light measurements are important indicators of asteroid taxonomy and can identify interesting targets for spectroscopic follow-up.

Key word: minor planets, asteroids: general

Online-only material: color figures, machine-readable table

1. INTRODUCTION

The *Wide-field Infrared Survey Explorer* (*WISE*; Wright et al. 2010) performed an all-sky survey in the thermal infrared, simultaneously imaging each field of view in four infrared wavelengths during the fully cryogenic portion of the mission and in the two shortest wavelengths when the mission continued as the Near-Earth Object *WISE* survey (*NEOWISE*; Mainzer et al. 2011a). The four *WISE* bandpasses are referred to as *W1*, *W2*, *W3*, and *W4*, and they cover the wavelength ranges of 3.1–3.8 μm , 4.1–5.2 μm , 7.6–16.3 μm , and 19.8–23.4 μm , respectively, with photometric central wavelengths of 3.4 μm , 4.6 μm , 12 μm , and 22 μm , respectively (Wright et al. 2010).

The single-frame *WISE*/*NEOWISE* data allow us to investigate the thermal emission and reflectance properties of the minor planets of the solar system. Due to their proximity to the Sun, near-Earth objects (objects with perihelia $q < 1.3$ AU) are typically dominated by thermal emission in *W2* (and occasionally even in *W1*), while, for more distant objects, *W2* measures a combination of reflected and emitted light and *W1* is dominated by reflected light. For all minor planets observed by *NEOWISE*, bands *W3* and *W4* are dominated by thermal emission.

Measurements of the thermal emission from asteroids can be used to determine the diameter of these bodies through the application of thermal models such as the Near-Earth Asteroid Thermal Model (*NEATM*; Harris 1998). *NEATM* assumes that the asteroid is a non-rotating sphere with no emission from the night side, and a variable beaming parameter (η) is used to account for variability in thermophysical properties and phase effects. *NEATM* provides a rapid method of determining diameter from thermal emission data that is reliable to $\sim 10\%$ when the beaming parameter can be fit (Mainzer et al. 2011c). Visible light measurements available from the Minor Planet Center (MPC)⁴

can then be combined with these models to constrain the geometric albedo at visible wavelengths (p_V). However, as these data are not simultaneous with the thermal infrared measurements, uncertainties due to rotation phase, observing geometry, and photometric phase behavior instill significant systematic errors in p_V determinations. The preliminary asteroid thermal fits presented in Mainzer et al. (2011b, 2012); Masiero et al. (2011, 2012a); Grav et al. (2011a, 2011b) for the near-Earth objects, main-belt asteroids, Hildas, and Jupiter Trojans account for these uncertainties in the determination of the optical H magnitude, resulting in a larger relative error on albedo than is found for diameter.

For objects that were observed by *NEOWISE* in both thermal emission and near-infrared (NIR) reflected light, we can simultaneously constrain the diameter as well as the NIR albedo. Because these data were taken at the same time and observing conditions as the thermal data used to model the diameter, no assumptions are needed regarding the photometric phase behavior of these objects, and light curve changes from rotation or viewing geometry do not contribute to the uncertainty. These NIR albedos will thus be a more precise indicator of the surface properties than the visible albedos.

The behavior of the NIR region of an asteroid's reflectance spectrum can be used as a probe of the composition of the surface. Spectra of asteroids in the NIR have been used for taxonomic classification (DeMeo et al. 2009), to constrain surface mineralogy (Gaffey et al. 2002; Reddy et al. 2012a), and to search for water in the solar system (Rivkin & Emery 2010; Campins et al. 2010). Near-infrared albedo measurements have also been used to identify candidate metal-rich objects in the NEO population (Harris & Drube 2014). Mainzer et al. (2011e) use the ratio of the NIR and visible albedos as a proxy for spectral slope and show a correspondence between this ratio and various taxonomic classifications. This relation was used by Mainzer et al. (2011b) to determine preliminary classifications

⁴ <http://www.minorplanetcenter.net>

Table 1
Revised Thermal Fits of Main-belt Asteroids

Name	Diameter (km)	η	p_V	p_{W1}	p_{W2}	H_V	G	Family
00005	108.29 ± 3.70	0.87 ± 0.10	0.27 ± 0.03	0.37 ± 0.03	0.20 ± 0.10	6.9	0.15	00005
00006	195.64 ± 5.44	0.91 ± 0.09	0.24 ± 0.04	0.35 ± 0.03	0.48 ± 0.32	5.7	0.24	...
00008	147.49 ± 1.03	0.81 ± 0.01	0.23 ± 0.04	0.38 ± 0.04	...	6.4	0.28	00008
00009	183.01 ± 0.39	0.86 ± 0.01	0.16 ± 0.03	0.33 ± 0.01	...	6.3	0.17	...
00009	184.16 ± 0.90	0.78 ± 0.01	0.16 ± 0.01	0.34 ± 0.04	...	6.3	0.17	...
00011	142.89 ± 1.01	0.78 ± 0.02	0.19 ± 0.02	0.35 ± 0.03	...	6.6	0.15	...
00012	115.09 ± 1.20	0.84 ± 0.02	0.16 ± 0.03	0.32 ± 0.02	...	7.3	0.22	00012
00014	140.76 ± 8.41	0.84 ± 0.15	0.27 ± 0.04	0.39 ± 0.06	0.19 ± 0.16	6.3	0.15	...
00015	231.69 ± 2.23	0.79 ± 0.04	0.25 ± 0.04	0.40 ± 0.04	...	5.3	0.23	00015
00017	84.90 ± 2.03	0.77 ± 0.04	0.19 ± 0.03	0.37 ± 0.08	...	7.8	0.15	...

(This table is available in its entirety in a machine-readable form in the online journal. A portion is shown here for guidance regarding its form and content.)

for NEOs, while Grav et al. (2011b, 2012) expanded upon this technique to taxonomically classify Hilda and Jupiter Trojan asteroids.

Masiero et al. (2011) presented NIR albedo measurements of main-belt asteroids assuming that the albedos at the W1 and W2 wavelengths were identical. However, for objects that have a sufficient number of detections of reflected light in multiple NIR bands, we can independently constrain each albedo (p_{W1} and p_{W2} for the W1 and W2 bandpasses, respectively). In this work, we present new thermal model fits of the NIR albedos of main-belt asteroids (MBAs), allowing p_{W1} and p_{W2} to vary independently. These albedos allow us to better distinguish different MBA compositional classes. They are also particularly useful for investigations of collisional families seen in the main belt, which show strongly correlated physical properties within each family.

2. DATA AND REVISED THERMAL FITS

To fit for NIR albedos of main-belt asteroids, we use data from the WISE/NEOWISE all-sky single exposure source table, which are available for download from the Infrared Science Archive (IRSA;⁵ Cutri et al. 2012). We extract photometric measurements of all asteroids observed by WISE following the technique described in Masiero et al. (2011) and Mainzer et al. (2011a). In particular, we use the NEOWISE observations reported to the MPC and included in the MPC’s minor planet observation database as the final validated list of reliable NEOWISE detections of solar system objects.

For objects with WISE detections in all four bands, we follow the fitting technique described in Grav et al. (2012) to independently determine the albedos in bands W1 and W2. This technique uses a faceted sphere with a temperature distribution drawn from the NEATM model to calculate the predicted visible and infrared magnitudes for each object. Diameter, beaming parameter, and visible W1 and W2 albedos are all varied until a best fit is found. Monte Carlo simulations of the data using the measurement errors then provide a constraint on the uncertainty of each parameter. We require at least three detections in each band above S/N = 4 to use that band in our fit. Main-belt asteroids are typically closer to the Sun at the time of observation than the Trojans and Hildas discussed in Grav et al. (2012), and thus the measured W2 flux can have a larger contribution of thermal emission for MBAs. Flux in the W1 band is typically

dominated by reflected light for MBAs observed by WISE, though low-albedo objects ($p_V < 0.1$) at heliocentric distances of $R_\odot < 2.5$ AU can be thermally dominated in W1 as well.

In order to ensure reliable fits for W2 albedos (p_{W2}), we require that the beaming parameter be fit by the model. The beaming parameter is a variable in the NEATM fit that consolidates uncertainties in the model due to viewing geometries and surface thermophysical parameters, and can be characterized as an enhancement of the thermal emission in the direction of the Sun. Changes in thermal properties or phase angles will lead to a range of possible beaming parameters for MBAs. In order to fit the beaming parameter, our model requires detections of thermal emission in two bands. We also require that the fraction of flux in W2 from reflected light be at least 10% of the total flux measured to fit p_{W2} . While this should be sufficient to constrain the W2 albedo in most cases, uncertainty in the beaming parameter can lead to large uncertainties in p_{W2} . To fit W1 albedo (p_{W1}), we followed the same procedure for p_{W2} , except now requiring the W1 reflected light to be at least 50% of the total flux. All objects that fulfilled the above requirements had optically measured magnitudes available in the literature, and thus allowed us to fit a visible albedo as well.

We present our updated thermal model fits for all objects satisfying the above constraints in Table 1, where we give the object’s name in MPC-packed format, absolute H_V magnitude and G photometric slope parameter from the MPC orbit file, associated family from Masiero et al. (2013) (or “...” if the object is not associated to a family), and our best fit and associated uncertainty on diameter, beaming parameter (η), p_{W1} , and p_{W2} if the latter could be constrained (“...” otherwise). Objects with two epochs of coverage have each epoch listed separately. All errors are statistical and do not include the systematic errors of ~10% on diameter and ~20% on visible albedo (see Mainzer et al. 2011c, 2011d; Masiero et al. 2011). Systematic errors will increase the absolute error on the fitted quantities, but do not affect relative comparisons within our sample, which is the main goal of this paper. This table contains 3080 fits of 2835 unique objects: 709 fits of 679 unique objects with constrained p_{W1} and p_{W2} ; 2371 fits of 2219 unique objects with only p_{W1} constrained; 63 objects that had one epoch where both NIR albedos were constrained and one epoch where only p_{W1} could be fit.

We note that some of the fits for diameter and beaming parameter (and thus albedo) are different from those presented in Masiero et al. (2011). Fits from NEATM using the same data set will give different values for the diameter as the beaming

⁵ <http://irsa.ipac.caltech.edu>

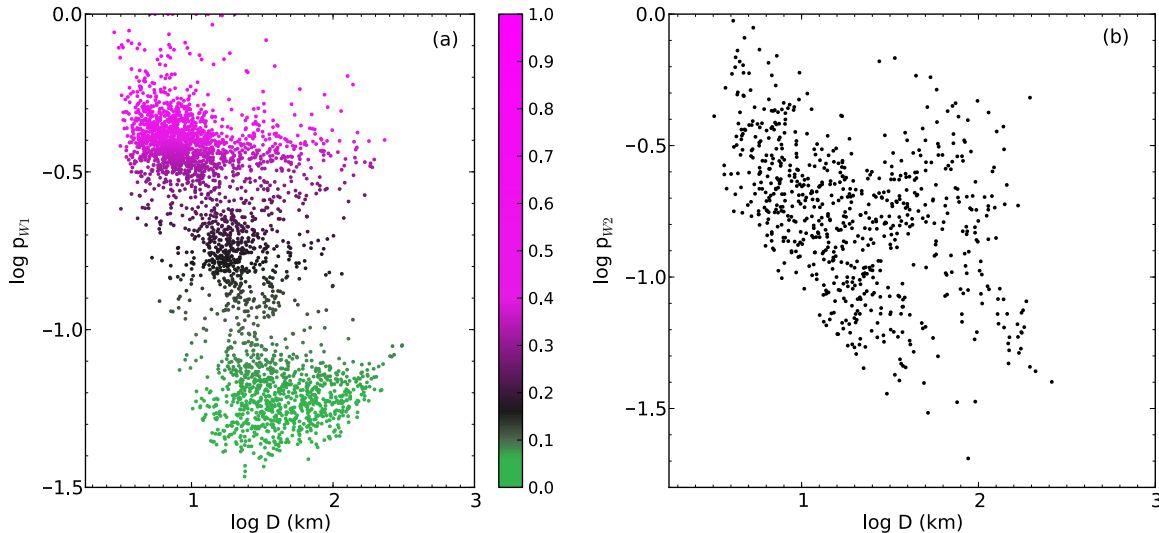


Figure 1. (a) W1 infrared albedo (p_{W1}) compared to fitted diameter, where color also indicates p_{W1} (as used in Figure 7). (b) W2 infrared albedo (p_{W2}) compared to diameter. Because the W1 and W2 detections are a measurement of reflected light, they are strongly biased by albedo. The dearth of small, low-albedo objects in this plot, which are observed in Masiero et al. (2011), is an artifact of this bias.

(A color version of this figure is available in the online journal.)

parameter is varied. In this case, by independently considering p_{W1} and p_{W2} , as opposed to averaging over both for a single value of p_{IR} , the calculated contribution of thermal flux in W2 will vary, which will result in a refined value of η and therefore diameter. For the majority of cases, diameters are consistent to within 10% of the previous value, visible albedos are consistent within 20%, and infrared albedo and beaming parameters are consistent within 15%. Revised beaming parameters tend to be $\sim 5\%$ smaller, making diameters $\sim 3\%$ smaller and visible albedos $\sim 6\%$ larger. W1 infrared albedos tend to increase $\sim 8\%$; however, we are not necessarily comparing similar quantities as the previous fits assumed that W1 and W2 albedos were equal, allowing W2 measurements to alter the best-fit value.

The criteria we apply to our fits, discussed above, result in selection effects in our sample that conspire to underrepresent the lowest albedo asteroids, as these objects are more likely to fall below our detectability threshold. This bias is a fundamental result of requiring reflected light observations in W1 and/or W2, but does not affect population surveys based on emission in W3 or W4. Our sample requirements also drive us to only use the data from the fully cryogenic portion of the WISE survey. It is possible to use fully cryogenic data to constrain the diameter and beaming parameter, and later measurements from either the NEOWISE post-cryo survey or the recently restarted NEOWISE mission (Mainzer et al. 2014) during a brighter apparition to constrain the NIR albedo properties (cf. Grav et al. 2012), although this technique requires a different method of handling that addresses difference in viewing geometry. We will apply this technique to main-belt asteroids in future work.

For objects with a sufficient number of detections in W1, but below our W2 sensitivity limit or our threshold for the fraction of reflected light in W2, we determine only the W1 albedo. These objects are either too small to reflect a detectable amount of light in W2, dominated by thermal emission in W2 (common for low-albedo objects, $p_{W1} < 0.1$), or have a blue spectral slope over the $3\text{--}5\ \mu\text{m}$ range and thus “drop out” of W2. Each of these scenarios will have a different implication for interpreting the distribution of W2 albedos, most notably that our data are least sensitive to smaller, lower albedo objects, as well as objects with blue $p_V\text{--}p_{W2}$ or $p_{W1}\text{--}p_{W2}$ spectral slopes. Interpretation of the

distribution of NIR albedos or spectral slopes, particularly as a function of taxonomy or size, must thus be made with the appropriate caveats. We also explore stacking of the predicted positions of these object in W2 to recover drop-out objects in future work.

3. DISCUSSION

3.1. Albedo Comparisons

Figure 1 shows p_{W1} and p_{W2} for all main-belt asteroids with sufficient data to constrain these parameters, compared to the fitted diameter. The W1 band is more sensitive than the W2 band (single-frame 5σ sensitivity of ~ 0.22 mJy versus ~ 0.31 mJy respectively; Cutri et al. 2012), and W1 detections are less frequently contaminated by thermal emission, which means we are able to measure p_{W1} for more asteroids than those with p_{W2} measurements (2835 versus 679). Both data sets show a strong bias against small, low-albedo asteroids, which is expected for data that require measurement of a reflected light component. A further bias against dark objects in p_{W2} due to rising thermal emission overtaking the small reflected light component is also present. From the data available, we see no evidence for a nonuniform distribution of p_{W2} , in contrast to p_{W1} , which shows three significant albedo clumps at $p_{W1} \sim 0.06$, $p_{W1} \sim 0.16$, and $p_{W1} \sim 0.4$.

Visible albedos for over 136,000 main-belt asteroids were presented in Masiero et al. (2011, 2012a). These measurements were based on the conversion of apparent visible magnitudes from a wide range of predominantly ground-based surveys to absolute H_V magnitudes when the orbit was determined by the MPC. Absolute magnitude is then converted to a predicted apparent magnitude during the epoch of the WISE/NEOWISE observations, often after assuming a photometric G parameter (see Bowell et al. 1989) and assuming that rotational variations are averaged over during the set of thermal infrared observations. These conversions and assumptions will instill additional uncertainty in the p_V determinations beyond what would be expected from uncertainties in the flux measurements and from thermal modeling. As a result, the fractional error on

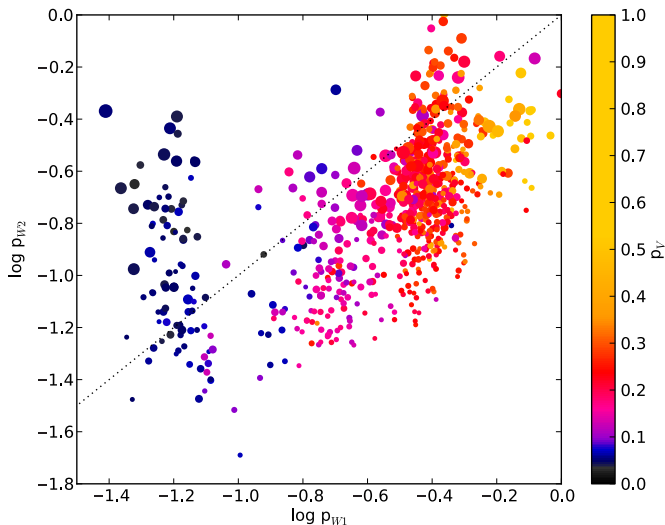


Figure 2. W2 albedo vs. W1 albedo for 679 main-belt asteroids. The color of the points indicate their visible albedo following the colormap presented in Masiero et al. (2011) and shown in the color bar, while the size of the point traces the fraction of the W2 flux that was due to reflected light. The dotted line shows a one-to-one correspondence; objects below the line will have a blue spectral slope from W1 to W2, while objects above the line will have a red slope.

(A color version of this figure is available in the online journal.)

p_V is typically 50%–100% larger than the fractional error on diameter from thermal model fits.

We compare the NIR albedos presented here to these visible albedos in Figures 2 and 3. For the majority of objects, p_{W1} traces p_V and can thus be used as an analog when p_V is not available. The uncertainties of the p_{W1} measurements in our data are smaller than the errors on p_V , and thus act as a better constraint of the surface properties. The relationship between p_{W2} and both p_V and p_{W1} is less distinct and varies over a large range of values for objects spanning high and low p_V and p_{W1} albedos.

Comparing the p_V distribution to Figure 10 from Masiero et al. (2011), we see that our sample contains significantly fewer low-albedo objects than would be expected from a random sample of all main-belt asteroids. The lack of low-albedo objects is due primarily to the observational selection effect imprinted on our data set by the requirement that the objects be detected in W1 and/or W2 in reflected light. This bias will increase as albedo decreases, preferentially selecting objects with higher albedos. A survey with deeper sensitivity in these wavelengths would allow us to probe smaller sizes at all albedos, but would still be subject to the same observational biases.

Following Grav et al. (2012), we can use our albedo measurements as a proxy for spectral slope from visible wavelengths through the NIR. Objects that fall above the one-to-one relationship in the top portion of Figure 3 will have a red spectral slope across the wavelengths plotted, while objects below this relation will have a blue spectral slope. As p_{W2} is the most poorly probed of the three parameters, there will be inherent detection biases against blue spectral slopes from objects that “drop out” and fall below our W2 detection threshold. For this reason, objects with the bluest slopes, particularly low-albedo objects, will be under-represented in our fits of p_{W2} .

To better compare the spectral slope information, in Figure 4, we show the difference in albedo between p_V , p_{W1} , and p_{W2} normalized to the measured p_{W1} value. Objects with positive values have a red spectral slope, while objects with negative values have a blue slope. High-albedo objects ($p_{W1} > 0.1$) tend

to show red slopes from visible to W1 wavelengths, and then blue slopes between W1 and W2. This behavior is similar to what is observed for Eucrite meteorites at these wavelengths (Reddy et al. 2012b), and what would be expected from extrapolating a typical S-type asteroid spectrum (DeMeo et al. 2009). High-albedo objects without a measured p_{W2} albedo show similar visible–W1 slopes to those with a measured p_{W2} .

Low-albedo objects ($p_{W1} < 0.1$) behave quite differently from their high-albedo counterparts. While slightly red from the visible to W1, these objects show a wide range of visible–W2 and W1–W2 slopes, from neutral in color to very red. An important caveat to this is shown by the objects without p_{W2} fits, which have slopes ranging from moderately red to significantly blue. Blue-sloped objects would be much fainter in W2 than W1 and thus would drop out from detection or be dominated by thermal emission in W2. It is probable that there is a population of these objects with blue W1–W2 slopes that are not represented in our plots. Extrapolating from the NIR spectra of low-albedo objects from DeMeo et al. (2009), we associate our objects that have red visible–W1 slopes with C-type and D-type objects. We can similarly associate the objects having blue-slopes with B-type asteroids; however, we note that only $\sim 1\%$ of objects studied by DeMeo et al. (2009) were identified as B-type asteroids, while $\sim 10\%$ of the asteroids in our study have low albedo and blue spectral slope. From Neese (2010), we find that the majority of our blue-sloped objects that have Bus–DeMeo taxonomic classifications are identified as B or Ch class objects, the latter of which represents a fraction of the spectroscopic sample comparable to the fraction of our sample in this group. Our blue slope may be indicative of the presence of mineralogical absorption features in the spectra of low-albedo objects at the wavelengths covered by W1.

3.2. D-type Asteroids

Asteroids with D-type taxonomic classifications become increasingly common as distance from the Sun grows, from the main belt through the Jupiter Trojan population (DeMeo & Carry 2013). These objects, especially the Jupiter Trojans, were likely implanted from a more distant reservoir during the early chaotic evolution of the solar system (Morbidelli et al. 2005) and thus represent primitive material distinct from objects that formed in the warmer region of the main belt. NIR albedo can be used to probe the distribution of these objects and differentiate between classes of primitive bodies. Grav et al. (2012) compare p_{W1} and p_{W2} to distinguish asteroids with D-type taxonomic classification from those with C- and P-type, and are able to determine the overall population fraction of D-type objects in the Jupiter Trojan and Hilda populations. They find that the majority of Jupiter Trojans are D-type at all sizes, while the Hilda population transitions from a minority of D-types at diameters $D > 40$ km to a majority at smaller sizes.

Following Grav et al. (2012), we show in Figure 5 an expanded view of the objects with lowest infrared albedos. We highlight the region of albedo space that is occupied by D-type asteroids in the Trojan and Hilda populations. The diameter and albedo fits from Grav et al. (2012) rely on the same model and assumptions as we use here, and thus comparisons between the two populations should only depend on the random error associated with the fits. Only 2% of all objects for which we measure p_{W1} and p_{W2} fall in this region; with the exception of (114) Cassandra and (267) Tirza (which are spectrally classified as T- and D-type objects, respectively), all other candidate D-type objects are in the outer main belt and have diameters

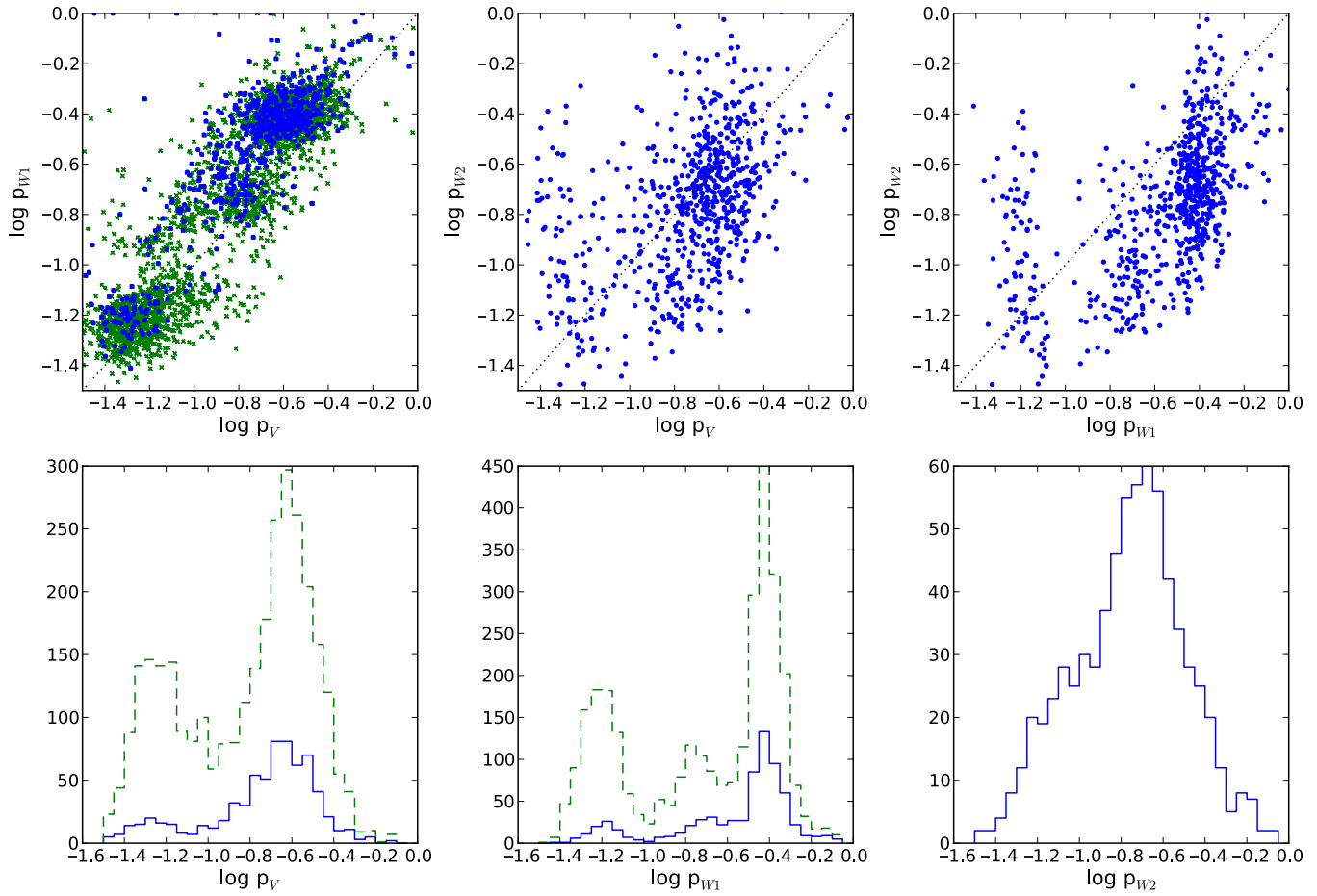


Figure 3. Comparisons (top) and histograms (bottom) of asteroid albedos at visible (p_V), W1 (p_{W1}), and W2 (p_{W2}) wavelengths. Blue points/lines show objects with all three albedos fit by the thermal model (679 objects), while green crosses/dashed lines show objects with only visible and W1 fits (2835 objects). Plots of p_{W2} do not include green crosses as these objects do not have this parameter constrained by the model fits. Dotted black lines in the comparison plots indicate a one-to-one relation. While visible and W1 albedos show clear clumping, W2 albedos show no separation within our measurement errors. (A color version of this figure is available in the online journal.)

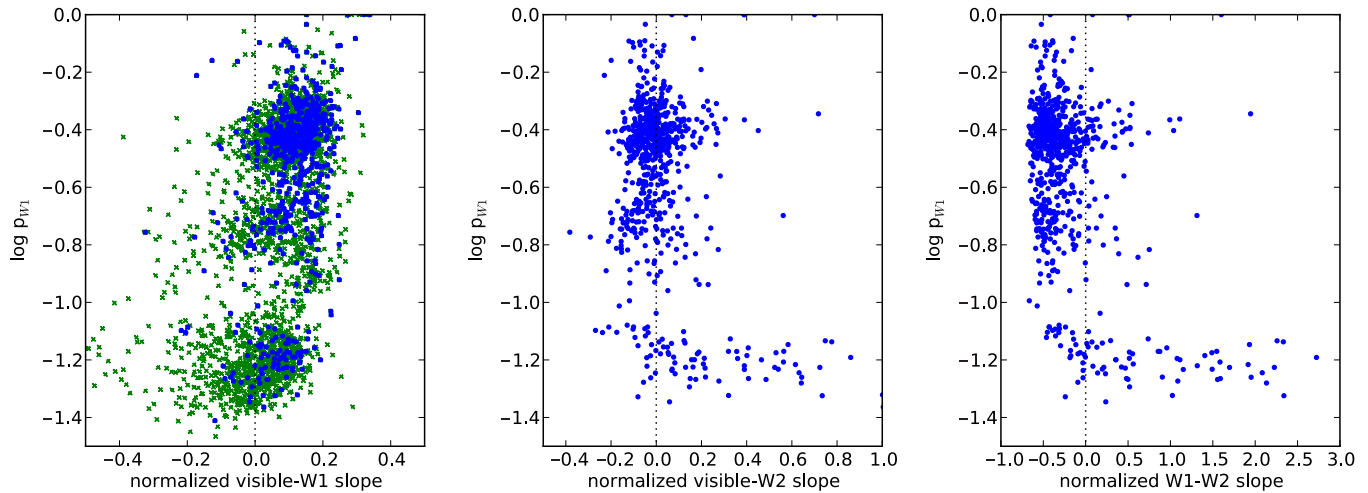


Figure 4. Spectral slope, normalized to the W1 albedo, over visible-to-W1 wavelengths (left), visible-to-W2 wavelengths (center) and W1-to-W2 wavelengths (right), compared to the W1 albedo. The dotted line shows a neutral slope; objects with positive slope values have red spectra and objects with negative values have blue spectra. High-albedo objects tend to be red-sloped from visible to W1 and blue-sloped from W1 to W2, while low-albedo objects tend to be flat or red across the whole range. The color and shape of the points are the same as those used in Figure 3. (A color version of this figure is available in the online journal.)

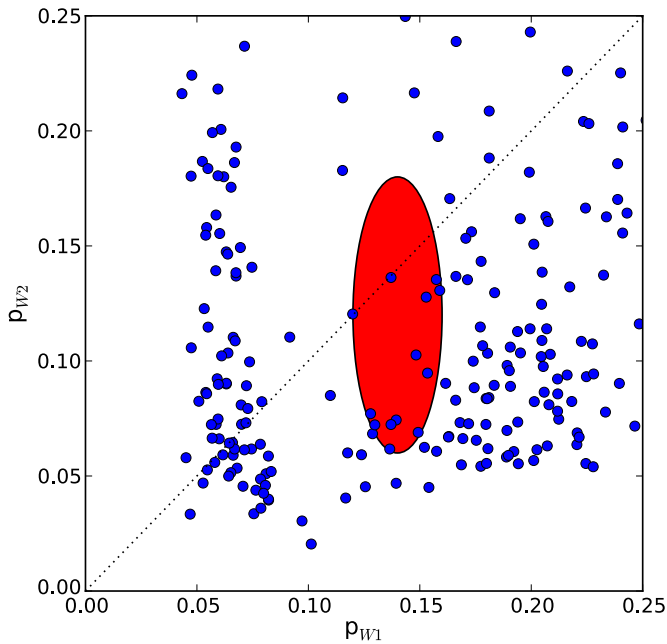


Figure 5. W1 and W2 albedos for all measured objects. The red ellipse marks the region populated by D-type asteroids as identified in Grav et al. (2012). This taxonomic classification shows no significant representation in the main-belt objects studied here.

(A color version of this figure is available in the online journal.)

between $10 \text{ km} < D < 40 \text{ km}$, consistent with the diameter regime where D-types dominate the Hilda asteroids. One object, (1755) Lorbach, is identified as an S-type in Neese (2010), but this classification relies on only two optical colors. For the outer main belt, we do not see a significant population of D-type objects like what is observed in the Hildas and Trojans (DeMeo & Carry 2013), but this is expected from the lower efficiency of dynamical implantation compared with the Hilda and Trojan populations Levison et al. (2009).

We find no objects in the inner main belt with albedos consistent with D-type objects. This is in contrast to the results of DeMeo et al. (2014) who find a small population of these bodies; however, this difference can be understood through the selection effects in our survey. Although our sample probes a large number of objects with semimajor axis, $a < 2.5 \text{ AU}$, only a handful have low albedo. Inner-main-belt low-albedo asteroids are more likely to have significant thermal emission in W2, thus we are not able to determine p_{W2} for these objects and they will not appear in our analysis.

3.3. Low- p_{W1} /High- p_{W2} Objects

Figure 5 shows a group of objects with low visible and W1 albedos ($p_V, p_{W1} < 0.1$) but high W2 albedo ($p_{W2} > 0.1$), which also appear as the objects with the reddest W1–W2 slopes in Figure 4. This class of object does not have an analog in the Jupiter Trojan or Hilda populations (Grav et al. 2012) where we find parallels to other low-albedo MBA populations. Objects from this group that have spectroscopic or photometric taxonomic classifications in PDS are typically designated as C-type or a related subclass (Neese 2010). There are occasional objects with other classifications such as X-, F-, and S-, or dual classifications. Though, in these cases, often the designation is based on only two color indices and thus is of low reliability. It is possible that this group could represent a different class of objects that is not found in the more distant solar system

populations, or instead could be a failure of the thermal model to converge for certain objects with low albedos.

In order to test if these objects are a result of a failure of the fitting routine, we take all objects in our fitted population with $p_{W1} < 0.1$ and compare the set with $p_{W2} \geq 0.1$ to the set with $p_{W2} < 0.1$ (referred to as “low–high” and “low–low,” respectively). The low–high and low–low test sets are approximately the same size (44 versus 48 objects) and have similar distributions of semimajor axes, eccentricities, inclinations, p_V , and p_{W1} . The primary difference between these two groups is that the low–high objects have significantly smaller heliocentric distances at the time of observation than the low–low objects, resulting in higher subsolar temperatures. The diameters of the low–high objects are also characteristically smaller than those of the low–low group; however, we cannot distinguish whether this is an actual difference between the groups or if it is a change in sensitivity as a result of the low–high objects being closer to the Sun and telescope at the time of observation, and thus warmer and brighter.

The asteroid (656) Beagle is a particularly interesting case for testing the differences between these two sets of objects. NEOWISE observed this asteroid at two different epochs, both while fully cryogenic, with good sensitivity at all four bands. One epoch of observations results in an NEATM best fit that falls into the low–low group, while the other epoch falls into the low–high group. The low–high epoch data were taken when Beagle was 0.21 AU closer to the Sun (2.82 AU versus 3.03 AU for the low–low case), following the trend seen for the overall population. The best fit for NEATM in the low–high epoch has a beaming parameter of $\eta = 1.46$ and a diameter of $D = 62 \text{ km}$ while the low–low epoch has best-fit values of $\eta = 1.03$ and $D = 48 \text{ km}$, which is the reverse of the diameter trend mentioned above. This large disagreement in diameter is not unexpected given the difference in the best-fit beaming parameter, which is inversely proportional to the fourth power of the subsolar temperature used in the NEATM model, and thus will change the model’s emitted flux.

The observations used for our fits were visually inspected, as well as compared to the WISE all-sky atlas of stationary sources, and show no significant contamination by background stars or galaxies. We note that (656) Beagle has a large amplitude lightcurve ($A > 1 \text{ mag}$) and a period of 7.035 hr (Menke 2005). Although large amplitudes can increase uncertainty in the fits, our data consist of 12 data points over 1 day and 15 data points over 1.25 days, thus both epochs cover multiple rotations. As such, light curve variations should be averaged over by our fits and should only contribute a small amount to the total uncertainty in the fit.

As a test of our model, we perform an NEATM fit using only bands W1, W2, and W3 as constraints, assuming that the W4 measurements are anomalously high, and a fixed beaming parameter of $\eta = 1.0$. When using a fixed beaming parameter, we cannot adequately constrain p_{W2} , thus we assume it is equal to p_{W1} . For these restricted fits, both epochs converge to diameters that agree to within 10%, but they cannot reproduce the measured magnitudes as well as the full-fit case. Because we are using one fewer constraint but two fewer variables, this is not surprising. The fits for (656) Beagle given by Masiero et al. (2011) are nearly identical to these restricted fits, but also cannot fully reproduce the measured magnitudes, particularly for the low–high epoch. Restricting our model further and only fitting W1 and W3, we find that both epochs converge to nearly identical diameters, and visible and infrared albedos.

We can understand these results by looking at where the best-fit model deviates from the data. For the low–high epoch, the full NEATM fit cannot simultaneously reproduce the $W2$, $W3$, and $W4$ fluxes simultaneously, with the $W2$ and $W4$ measurements showing excesses not observed in $W3$. Our full model finds a best-fit solution allowing $W3$ and $W4$ to determine the diameter and beaming, which under-produces flux in $W2$, but corrects that by increasing p_{W2} . If we ignore the $W4$ measurements, the $W2$ and $W3$ fluxes still cannot be reproduced in the low–high epoch solely with thermal emission and reflected light without resorting to extreme changes in p_{W2} .

One possible explanation for the disagreement between epochs is that we are observing significant differences between the thermal emission in the morning and afternoon hemispheres of the asteroid. If (656) Beagle has a relatively high thermal inertia, then there may be a significant lag to the thermal re-emission of incident light that is not accounted for in the NEATM model. Our two epochs of observation are at phase angles of $\alpha \sim 20^\circ$, but on opposite sides of the body. (656) Beagle is on a low-inclination orbit, thus if we assume the rotation pole is oriented perpendicular to the orbital and ecliptic planes and that the rotation is prograde, then the data from the low–high epoch would correspond to the afternoon hemisphere and the data from the low–low epoch would correspond to the morning hemisphere. Future work will implement a full thermophysical model of this object to test if the $W2$ and $W4$ excesses can be explained by a morning/afternoon dichotomy. For all other objects in the low–high group, which were only observed at a single epoch, we cannot currently differentiate between poor fits to the beaming parameter and actual excesses in the $W2$ and/or $W4$ bands.

An alternate possibility is that these fits are indicative of problems with the flux measurement of partially saturated sources in the *WISE* data. Cutri et al. (2012) discuss the process by which fluxes are measured for saturated sources through PSF-fitting photometry. Flux measurements are available for sources many magnitudes above the brightness where the central pixel saturates through fitting of the PSF wings; however, for very bright sources in bands $W2$ and $W3$, there appears to be a slight over estimation of the fluxes. None of the objects we fit here had $W2$ magnitudes in this saturated regime; however, the majority of objects with $p_{W1} < 0.1$ had $W3$ magnitudes in this problematic region.

We correct for saturation estimation issues in our thermal model; however, there is potential that the error for asteroidal sources cannot be adequately described by this correction, which was calibrated for stars. The difference in the spectral energy distributions through the $W3$ bandpass of hot, blue stars and cooler, red asteroids could potentially result in differences deep in the wings of the PSF for each type of source that is not fully encompassed by the color correction. These subtle changes can have a significant impact on saturated sources where only the wings are available for profile fitting; however, there are an insufficient number of well-calibrated, $W3$ -bright sources with the appropriate spectral energy distribution to correct for this effect. Although this error may only have a small effect on other physical parameters within our modeled systematic uncertainties, due to $W2$'s position on the Wien's side of main-belt asteroid thermal emission for some of our objects, a small change in $W3$ can result in a large change in $W2$ flux, and thus our interpretation of the $W2$ albedo. As such, caution is strongly encouraged when interpreting fits for objects with very bright $W3$ magnitudes ($W3 < 4$ mag).

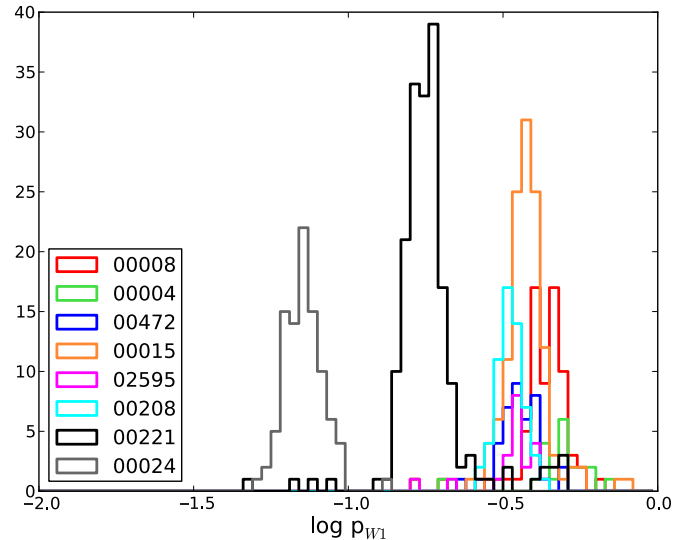


Figure 6. $W1$ albedo distributions for 8 asteroid families with more than 20 measured NIR albedos, identified by the family ID given in Masiero et al. (2013) and Table 2. Families show narrow distributions of albedos correlating with one of three major albedo groupings.

(A color version of this figure is available in the online journal.)

3.4. NIR Albedos of Asteroid Families

The distributions of visible albedos for members of each asteroid family have much narrower spread than the albedo distribution of the main belt as a whole (Masiero et al. 2011), which is expected from a population resulting from the collisional breakup of a single parent body. As the (4) Vesta family shows a narrow albedo distribution but originated from a differentiated body, we do not expect the albedo distributions of other cratering-event families that may have been partially or fully melted to differ significantly from nondifferentiated families. It is possible that families formed from the complete disruption of a differentiated parent body may show a broader albedo distribution, though we do not see any evidence for a case like this in our data. Visible albedo can also be used to improve family membership lists by rejecting outlier objects that are dynamically similar to the family (Masiero et al. 2013; Walsh et al. 2013). Using the refined family lists from Masiero et al. (2013), we investigate the distribution of p_{W1} for families as a more accurate tracer of the surface properties of these asteroids.

Figure 6 shows the distribution of p_{W1} albedos for the 8 families where more than 20 members had a p_{W1} albedo measurement. Asteroid families break into three clear groupings, following the three peaks in the albedo distribution shown in Figure 3. Our data set depends on reflected light measurements, so high-albedo families are over-represented in the distribution compared with the population of all known families, which is dominated by low-albedo families. The only low NIR-albedo family with more than 20 measured objects was (24) Themis; however, other families such as (10) Hygiea, (145) Adeona, (276) Adelheid, (511) Davida, (554) Peraga (equivalent to other lists' Polana family), and (1306) Scythia also show low NIR albedos, but these families contain only a small number of objects with measured p_{W1} . The families (4) Vesta, (8) Flora, (15) Eunomia, (208) Lacrimosa, (472) Roma, and (2595) Gudiachvili all have high p_{W1} and show only a small spread in mean albedo, while (135) Hertha (equivalent to other lists' Nysa family) and (254) Augusta join them at a lower significance level.

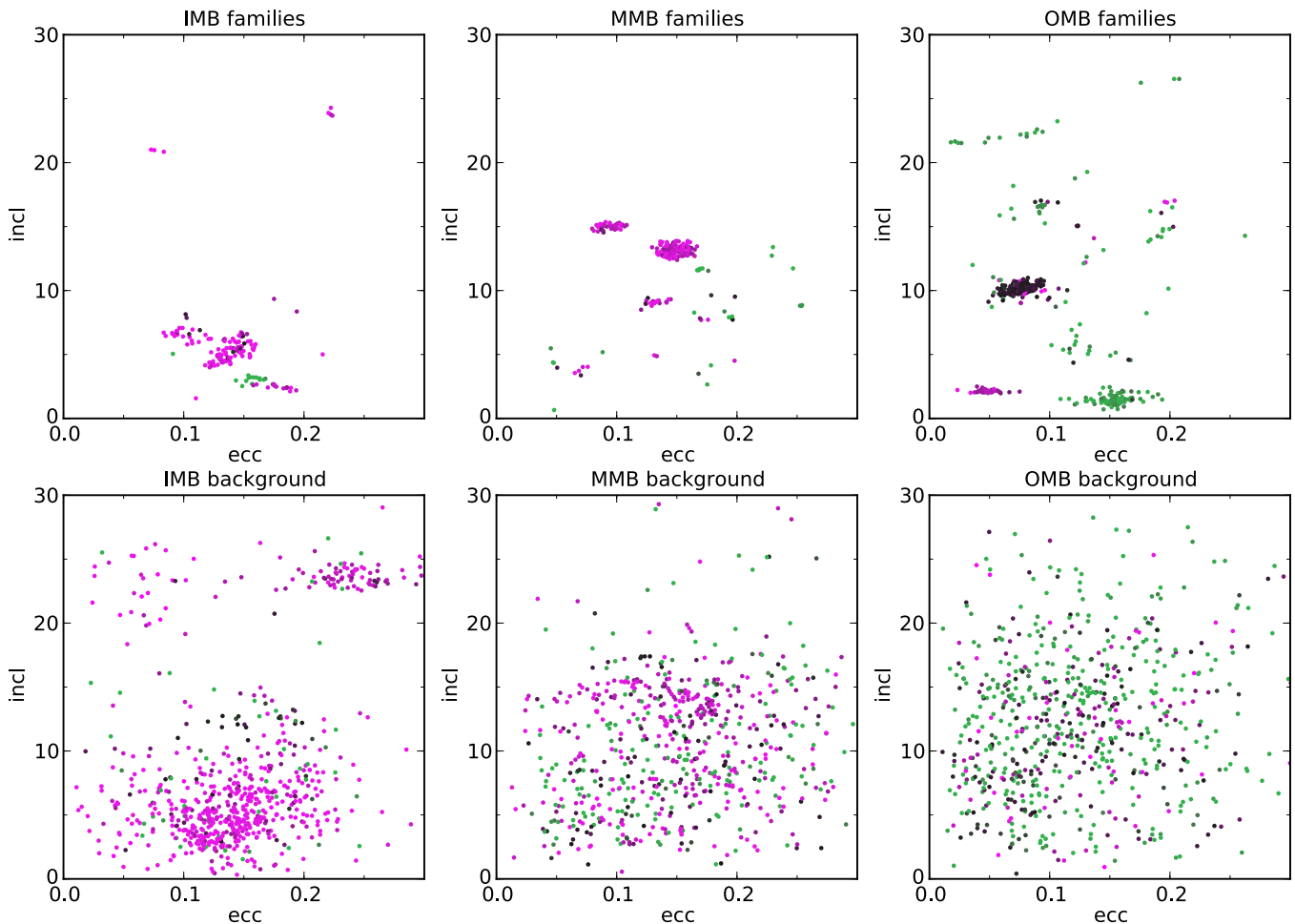


Figure 7. Proper orbital inclination (incl) vs. eccentricity (ecc) for (left) inner, (center) middle, and (right) outer main belt populations, (top) for objects associated with families and (bottom) background objects not linked to families. The colors of the points map the p_{W1} albedo (from green to black to magenta for increasing p_{W1}), following Figure 1(a).

(A color version of this figure is available in the online journal.)

The (221) Eos family is the only one of the large families to have a moderate NIR albedo in between the high- and low-albedo populations, indicating that this family has surface properties that are rare among the large main-belt asteroids. The p_{W1} values for this family confirm the observed moderate visible albedo as a separate grouping that could not be conclusively distinguished from the high p_V population by Masiero et al. (2013). The Eos family parent has a K-type spectral taxonomy in the Bus–DeMeo system (DeMeo et al. 2009). K-type objects are considered “end-members” of the classification scheme, and have a $1 \mu\text{m}$ absorption feature typically associated with silicates such as olivine, but are distinct in spectroscopic principal component space from the majority of S-class objects. Clark et al. (2009) and Hardersen et al. (2011) associate K-type objects with the parent body of carbonaceous chondrite meteorites, specifically CO chondrites, while Mothé-Diniz (2005) show evidence that (221) Eos may have been partially differentiated. Broz & Morbidelli (2013) calculate the time since the breakup of the (221) Eos family as 1.5–1.9 Gyr, making it one of the oldest main-belt families with a measured age. These observed properties, when taken together, paint the Eos family as having a unique evolutionary history that can be studied using remote observations in combination with hand samples from the meteorite record to trace the early history of the solar system.

We note that approximately half of the objects fit for the (298) Baptistina family had albedos similar to the Eos family, while the remainder appear to be drawn from the high-albedo group. This result is based on only a small number of measured Baptistina members, and thus is not conclusive; however, if confirmed, it would further impede attempts to assign a unique composition to this family (see Reddy et al. 2011) or determine its age and evolution (see Masiero et al. 2012b).

Figure 7 shows the proper orbital eccentricity and inclination of all objects with measured p_{W1} . The main belt is split into three regions by proper semi-major axis (a): the inner main belt (IMB; $1.8 \text{ AU} < a < 2.5 \text{ AU}$), the middle main belt (MMB; $2.5 \text{ AU} < a < 2.82 \text{ AU}$), and the outer main belt (OMB; $2.82 \text{ AU} < a < 3.6 \text{ AU}$). We show separately the objects that were associated with an asteroid family by Masiero et al. (2013) and those that are members of the background population. The (221) Eos family stands out distinctly in the belt, though objects with similar p_{W1} are present in the background population in all three regions.

These plots show the clear trend of albedo decreasing with distance from the Sun; however, our observational bias against small, low albedo objects amplifies this effect. Broz et al. (2013), Carruba et al. (2013), and Masiero et al. (2013) observe halos of objects beyond the limits of typical family-identification techniques; however, we do not see evidence for these halos

Table 2
Average Orbital and Physical Properties for Asteroid Family Members with Measured p_{W1}

Family	Semimajor Axis (AU)	Eccentricity	Inclination (deg)	D_{\max} (km)	D_{\min} (km)	$\langle p_V \rangle$	$\langle p_{W1} \rangle$	Sample Size
00434	1.937	0.077	20.947	7.62	3.01	0.725 ± 0.172	0.736	3
00254	2.197	0.122	4.202	11.85	5.71	0.298 ± 0.105	0.420	7
00008	2.244	0.141	5.251	155.74	3.86	0.291 ± 0.091	0.435 ± 0.074	70
00298	2.256	0.148	5.723	12.32	5.36	0.146 ± 0.034	0.284	9
00163	2.325	0.215	5.008	4.78	...	0.053 ± 0.016	0.401	1
00587	2.338	0.222	23.901	12.23	4.41	0.310 ± 0.090	0.421	4
01646	2.353	0.102	8.002	12.47	11.57	0.204 ± 0.081	0.221	2
00004	2.366	0.101	6.518	109.51	4.53	0.357 ± 0.110	0.466 ± 0.129	22
00012	2.390	0.185	8.853	126.64	7.62	0.066 ± 0.021	0.318	2
00135	2.405	0.178	2.455	82.15	3.77	0.280 ± 0.088	0.372 ± 0.071	13
00302	2.407	0.110	1.576	6.11	...	0.062 ± 0.021	0.422	1
00554	2.418	0.157	3.049	55.18	11.75	0.061 ± 0.021	0.054 ± 0.012	13
00752	2.463	0.091	5.049	60.85	...	0.053 ± 0.014	0.048	1
13698	2.469	0.118	6.534	5.31	...	0.367 ± 0.098	0.412	1
01658	2.560	0.172	7.749	13.81	5.97	0.255 ± 0.074	0.343	3
00472	2.562	0.094	15.009	47.04	6.25	0.261 ± 0.079	0.363 ± 0.051	39
00005	2.576	0.198	4.514	113.00	...	0.240 ± 0.105	0.365	1
00606	2.587	0.179	9.631	39.53	...	0.117 ± 0.028	0.137	1
05079	2.601	0.247	11.730	14.76	...	0.068 ± 0.020	0.047	1
00404	2.628	0.229	13.062	105.41	73.07	0.060 ± 0.025	0.059	2
00015	2.630	0.149	13.181	299.21	4.45	0.263 ± 0.084	0.382 ± 0.073	126
00569	2.634	0.175	2.659	13.18	...	0.054 ± 0.016	0.064	1
00145	2.676	0.170	11.642	132.59	14.70	0.062 ± 0.018	0.055	8
00410	2.727	0.253	8.824	27.28	8.49	0.085 ± 0.028	0.075	3
00539	2.739	0.164	8.274	56.04	...	0.061 ± 0.023	0.039	1
00396	2.742	0.168	3.497	37.29	...	0.093 ± 0.024	0.115	1
00808	2.744	0.132	4.902	37.68	9.51	0.232 ± 0.071	0.380	2
00363	2.750	0.045	5.480	19.34	...	0.068 ± 0.018	0.079	1
00128	2.750	0.088	5.181	193.08	...	0.075 ± 0.024	0.071	1
01734	2.769	0.194	7.951	23.82	8.72	0.056 ± 0.017	0.074	6
00847	2.777	0.070	3.742	30.08	8.78	0.218 ± 0.075	0.359	5
00272	2.783	0.048	4.232	25.67	21.09	0.047 ± 0.014	0.109	3
00322	2.783	0.198	9.521	73.15	...	0.078 ± 0.027	0.193	1
01128	2.788	0.048	0.659	48.63	...	0.048 ± 0.013	0.046	1
02595	2.791	0.132	9.068	14.62	6.59	0.262 ± 0.075	0.343 ± 0.059	21
01668	2.806	0.178	4.152	25.83	...	0.052 ± 0.014	0.048	1
03985	2.851	0.123	15.052	22.11	16.19	0.176 ± 0.058	0.213	3
00081	2.854	0.180	8.233	123.96	...	0.056 ± 0.016	0.053	1
00208	2.875	0.048	2.129	49.99	10.36	0.237 ± 0.063	0.335 ± 0.032	59
00845	2.940	0.036	11.999	58.53	...	0.061 ± 0.017	0.055	1
00179	2.972	0.076	9.027	74.58	...	0.223 ± 0.069	0.326	1
00816	3.004	0.145	13.168	50.09	...	0.051 ± 0.026	0.054	1
00221	3.020	0.077	10.181	95.62	10.03	0.158 ± 0.048	0.190 ± 0.065	186
00283	3.070	0.109	8.917	145.55	17.68	0.048 ± 0.019	0.084	2
02621	3.086	0.128	12.128	47.92	...	0.081 ± 0.029	0.066	1
01113	3.112	0.137	14.093	48.37	...	0.074 ± 0.031	0.350	1
00780	3.117	0.070	18.186	114.26	...	0.056 ± 0.018	0.060	1
01040	3.122	0.197	16.728	22.67	7.56	0.225 ± 0.075	0.348	4
00511	3.138	0.192	14.439	285.84	23.46	0.065 ± 0.026	0.076	8
00024	3.142	0.153	1.457	193.54	17.43	0.068 ± 0.021	0.073 ± 0.012	95
00928	3.143	0.193	16.359	62.54	24.29	0.075 ± 0.038	0.057	2
00010	3.143	0.130	5.514	153.58	16.69	0.070 ± 0.023	0.079 ± 0.035	17
03330	3.154	0.199	10.149	15.49	...	0.044 ± 0.015	0.053	1
00490	3.165	0.061	9.323	79.87	...	0.069 ± 0.022	0.050	1
00778	3.169	0.262	14.282	19.36	...	0.066 ± 0.020	0.070	1
01306	3.170	0.091	16.448	72.24	15.54	0.061 ± 0.021	0.107 ± 0.056	14
00031	3.177	0.196	26.445	281.98	17.31	0.057 ± 0.016	0.068	3
00618	3.189	0.058	15.879	131.23	...	0.056 ± 0.018	0.063	1
00702	3.190	0.021	21.598	196.47	26.15	0.066 ± 0.022	0.071	3
00276	3.190	0.072	22.189	100.36	21.98	0.068 ± 0.022	0.073 ± 0.009	11
01303	3.215	0.126	19.023	102.43	28.58	0.049 ± 0.017	0.069	2
00087	3.485	0.054	9.846	288.38	...	0.057 ± 0.017	0.082	1

Note. Mean p_V values are taken from Masiero et al. (2013).

in the background population in our data set. Halos are typically associated with asteroids that have dispersed a large distance from the family center via Yarkovsky and gravitational forces, which will have smaller diameters than objects that were above our sensitivity limit for p_{W1} determination. Our sample size, which is significantly smaller than what is typically used in surveys investigating family halos, may also contribute to their absence in our data.

In Table 2, we present the orbital and physical properties for all families identified in Masiero et al. (2013) that had at least one member with a fitted NIR albedo. We list the name of the family, the average proper orbital elements, the largest (D_{\max}) and smallest diameter (D_{\min}) represented in our sample, the $W1$ albedos with standard deviations, and the number of family members with data sufficient to fit. For reference, we also provide the mean, p_V , and standard deviation from Masiero et al. (2013). For cases where only a single body had a measured p_{W1} (often but not always the parent body of the family), D_{\min} is marked with a “...” entry and no standard deviation is given for the mean $W1$ albedo for families with less than 10 members. Asteroids that have been incorrectly associated with families may have very different mineralogies and thus spectral behavior in the NIR, which could make those objects more likely to fulfill the selection requirements for measured p_{W1} . Thus, particular caution is necessary when dealing with families suffering small number statistics, especially families with only a single p_{W1} -fit object. We note that the mean p_V albedos presented in Masiero et al. (2013) are based on larger numbers of objects and so will generally be more accurate than the mean p_{W1} values given here.

It is also possible to use the $W1$ albedo to further refine family memberships, particularly for confused cases such as the Nysa–Polana complex. Masiero et al. (2013) divided this complex into a high-albedo component with largest body (135) Hertha and a low-albedo component with largest body (554) Peraga, which is nearly twice the diameter of (142) Polana. We use the NIR albedo to reject objects from the low-albedo family that had moderate visible albedos but $W1$ albedos characteristic of the high-albedo family. Asteroids (261), (1823), (2717), and (15112) can thus be rejected as members of the (554) Peraga group based on the $W1$ albedo. We note that because of a typo in Masiero et al. (2013) (135) Hertha was mistakenly listed as associated with (554) Peraga instead of with its own family, which we correct here. Walsh et al. (2013) present dynamical arguments to divide the (554) Peraga family into two sub-families; however, we are unable to see any distinction between these groups in either the visible or $W1$ albedo.

4. CONCLUSIONS

We present revised thermal model fits for main-belt asteroids, allowing for the albedo in each of the near-infrared reflected wavelengths to be fit independently. The $3.4 \mu\text{m}$ and $4.6 \mu\text{m}$ spectral regions covered by the *WISE*/NEOWISE $W1$ and $W2$ bandpasses are poorly probed in ground-based spectroscopy, but can be used to provide insight into asteroid mineralogical composition by constraining spectral slope. In total, we present 3080 fits of p_{W1} and/or p_{W2} for 2835 unique main-belt objects.

The MBA population has three distinct peaks in our observed p_{W1} distribution at $p_{W1} \sim 0.06$, $p_{W1} \sim 0.16$, and $p_{W1} \sim 0.4$. The high and low p_{W1} peaks correspond to the high and low visible albedo groups previously observed, while the moderate p_{W1} peak corresponds to an intermediate visible albedo that is

blended with the high p_V objects in visible albedo distributions. The distribution of albedos that we measure have a larger fraction of high-albedo objects than what was observed for the MBA visible albedo distribution; however, this is an effect of the biases in our sample selection.

Asteroid families have narrow p_{W1} distributions corresponding to one of the three observed p_{W1} peaks. The (221) Eos family represents the only significant concentration of objects near the peak at $p_{W1} \sim 0.16$, though other objects with this albedo, which are not related to asteroid families, are scattered throughout the entire main-belt region. This family also corresponds to an unusual “end member” taxonomic classification, K-type, that has been suggested to correspond to a partially differentiated parent or olivine-rich mineralogy. NIR albedo measurements provide a way to rapidly search the known population for candidate K-type objects in the main belt, and are a powerful tool that acts as a proxy for asteroid taxonomic type.

Our results show that the majority of high-albedo objects, believed to have surface compositions dominated by silicates and similar to ordinary chondrite meteorites, show an overall reddening from visible to $W1$ wavelengths similar to what is seen in the NIR. The spectra become blue from $W1$ to $W2$, which is also seen in some meteorite populations, particularly the Eucrites. This overall picture is consistent with a primarily silicate dominated composition. Objects with moderate infrared albedos show similar behavior across the wavelengths probed here, though the lower albedo value at $W1$ may indicate subtle differences in composition from the high-albedo population or even a mix of different mineralogies.

The low-albedo objects in our sample show a much wider range of behavior in these spectral regions. Many objects show red slopes across all wavelengths, consistent with the NIR spectral behavior of C/D/P-type objects. However, approximately 10% of our population show a blue slope from visible to $W1$, even in spite of the biases against blue-sloped, low-albedo objects in our sample. These objects are associated with B and Ch spectral taxonomies. The blue visible-to- $W1$ spectral slope in the Ch class objects may be indicative of a significant absorption feature at $W1$ wavelengths from minerals such as carbonates.

The fits presented here are based on reflected light, and thus our sample will not accurately represent the true distribution of p_{W1} or p_{W2} . Small, low-albedo asteroids as well as objects with blue NIR spectral slopes are more likely to be undetected in the $W1$ and/or $W2$ wavelengths and thus underrepresented in our population distributions. A larger survey with greater sensitivity in these spectral regions is required to extend these results to a population comparable to the one with measured diameters and visible albedos.

J.M. was partially supported by a NASA Planetary Geology and Geophysics grant. C.N., R.S., and S.S. were supported by an appointment to the NASA Postdoctoral Program at JPL, administered by Oak Ridge Associated Universities through a contract with NASA. We thank the referee for helpful comments that greatly improved this manuscript. This publication makes use of data products from the *Wide-field Infrared Survey Explorer*, which is a joint project of the University of California, Los Angeles, and the Jet Propulsion Laboratory/California Institute of Technology, funded by the National Aeronautics and Space Administration. This publication also makes use of data products from NEOWISE, which is a project of the Jet Propulsion Laboratory/California Institute of Technology, funded by the Planetary Science Division of the National

Aeronautics and Space Administration. This research has made use of the NASA/IPAC Infrared Science Archive, which is operated by the Jet Propulsion Laboratory, California Institute of Technology, under contract with the National Aeronautics and Space Administration.

REFERENCES

- Bowell, E., Hapke, B., Domingue, D., et al. 1989, *Asteroids II* (Tucson, AZ: Univ. Arizona Press), 524
- Broz, M., & Morbidelli, A. 2013, *Icar*, 223, 844
- Broz, M., Morbidelli, A., Bottke, W. F., et al. 2013, *A&A*, 551, A117
- Campins, H., Hargrove, K., Pinilla-Alonso, N., et al. 2010, *Natur*, 464, 1320
- Carruba, V., Domingos, R. C., Nesvorný, D., et al. 2013, *MNRAS*, 433, 2075
- Clark, B. E., Ockert-Bell, M. E., Cloutis, E. A., et al. 2009, *Icar*, 202, 119
- Cutri, R. M., Wright, E. L., Conrow, T., et al. 2012, Explanatory Supplement to the WISE All-Sky Data Release Products, <http://wise2.ipac.caltech.edu/docs/release/allsky/expsup/index.html>
- DeMeo, F. E., Binzel, R. P., Slivan, S. M., & Bus, S. J. 2009, *Icar*, 202, 160
- DeMeo, F. E., Binzel, R. P., Carry, B., Polishook, D., & Moskovitz, N. A. 2014, *Icar*, 229, 392
- DeMeo, F. E., & Carry, B. 2013, *Icar*, 226, 723
- Gaffey, M. J., Cloutis, E. A., Kelley, M. S., & Reed, K. L. 2002, in *Asteroids III*, ed. W. F. Bottke, Jr., A. Cellino, P. Paolicchi, & R. P. Binzel (Tucson, AZ: Univ. Arizona Press), 183
- Grav, T., Mainzer, A., Bauer, J., et al. 2011a, *ApJ*, 742, 40
- Grav, T., Mainzer, A., Bauer, J., et al. 2011b, *ApJ*, 744, 197
- Grav, T., Mainzer, A. K., Bauer, J. M., Masiero, J. R., & Nugent, C. R. 2012, *ApJ*, 759, 49
- Hardersen, P. S., Cloutis, E. A., Reddy, V., et al. 2011, *M&PS*, 46, 1910
- Harris, A. W. 1998, *Icar*, 131, 291
- Harris, A. W., & Drube, L. 2014, *ApJL*, 785, L4
- Levison, H. F., Bottke, W. F., Gounelle, M., et al. 2009, *Natur*, 460, 364
- Mainzer, A. K., Bauer, J. M., Grav, T., et al. 2011a, *ApJ*, 731, 53
- Mainzer, A. K., Bauer, J. M., Grav, T., et al. 2014, *ApJ*, in press (arXiv:1406.6025)
- Mainzer, A. K., Grav, T., Bauer, J. M., et al. 2011b, *ApJ*, 743, 156
- Mainzer, A. K., Grav, T., Masiero, J., et al. 2011c, *ApJ*, 736, 100
- Mainzer, A. K., Grav, T., Masiero, J., et al. 2011d, *ApJL*, 737, 9
- Mainzer, A. K., Grav, T., Masiero, J., et al. 2011e, *ApJ*, 741, 90
- Mainzer, A. K., Grav, T., Masiero, J., et al. 2012, *ApJL*, 760, 12
- Masiero, J. R., Mainzer, A. K., Bauer, J. M., et al. 2013, *ApJ*, 770, 7
- Masiero, J. R., Mainzer, A. K., Grav, T., et al. 2011, *ApJ*, 741, 68
- Masiero, J. R., Mainzer, A. K., Grav, T., et al. 2012, *ApJL*, 759, L8
- Masiero, J. R., Mainzer, A. K., Grav, T., Bauer, J. M., & Jedicke, R. 2012, *ApJ*, 759, 14
- Menke, J. 2005, *MPBu*, 32, 85
- Morbidelli, A., Levison, H. F., Tsiganis, K., & Gomes, R. 2005, *Natur*, 435, 462
- Mothé-Diniz, T., & Carvano, J. M. 2005, *A&A*, 442, 727
- Neese, C. (ed.) 2010, Asteroid Taxonomy V6.0. EAR-A-5-DDR-TAXONOMY-V6.0. NASA Planetary Data System, <http://sbn.psi.edu/pds/resource/taxonomy.html>
- Reddy, V., Carvano, J. M., Lazzaro, D., et al. 2011, *Icar*, 216, 184
- Reddy, V., Nathues, A., Le Corre, L., et al. 2012a, *Sci*, 336, 700
- Reddy, V., Sanchez, J., Nathues, A., et al. 2012b, *Icar*, 217, 153
- Rivkin, A. S., & Emery, J. P. 2010, *Natur*, 464, 1322
- Walsh, K. J., Delbó, M., Bottke, W. F., Vokrouhlický, D., & Lauretta, D. S. 2013, *Icar*, 225, 283
- Wright, E. L., Eisenhardt, P., Mainzer, A. K., et al. 2010, *AJ*, 140, 1868